Silicon (2024) 16:2005–2021
https://doi.org/10.1007/s12633-023-02811-x

RESEARCH

Numerical Simulation and Design of All-Thin-Film Homojunction Perovskite/c-Si Tandem Solar Cells

Omar M. Saif[1,2] · Ahmed Shaker[3] · Mohamed Abouelatta[1] · Abdelhalim Zekry[1] · Yasmine Elogail[4]

Received: 12 September 2023 / Accepted: 2 December 2023 / Published online: 13 December 2023

Abstract

Double-junction solar devices featuring wide-bandgap and narrow-bandgap sub-cells are capable of boosting performance and efficiency compared to single-junction photovoltaic (PV) technologies. To achieve the best performance of a double-junction device, careful selection and optimization of each sub-cell is crucial. This work presents the investigation of an all-thin-film two-terminal (2T) monolithic homojunction perovskite (PVK)/c-Si tandem cell using Silvaco TCAD simulation. The front sub-cell utilizes homojunction PVK that has a bandgap of 1.72 eV, whereas the rear sub-cell uses thin c-Si with a bandgap of 1.12 eV. Both cells are connected via a p^{++}/n^{++} silicon tunnel diode. Experimental calibration of the heterojunction PVK and c-Si cells yields power conversion efficiencies (PCE) of 18.106% and 17.416%, respectively. When integrated into an initial PVK/c-Si tandem, the resulting cell achieves a PCE of 29.38%. To compare the performance, the heterojunction PVK layer is replaced with an *n-p* homojunction PVK layer, revealing the impact of the absence of a surplus built-in electric field in the perovskite film as a strong limiting factor. Further, a thorough investigation of four distinct structures for the *n-p* homojunction PVK cell is conducted. The four structures include a complete cell, electron transport layer (ETL)-free, hole transport layer (HTL)-free, and carrier transport layer (CTL)-free structures. The results show that the CTL-free structure has significant potential after applying certain optimization techniques that result in reducing surface recombination, enhancing the built-in electric field, and improving light absorption. With the current-matching condition achieved, the tandem efficiency reaches 36.37%.

Keywords All-thin-film · Homojunction · Perovskite · Thin-film c-Si · CTL-free · Tandem · Current matching

✉ Ahmed Shaker
ahmed.shaker@eng.asu.edu.eg

Omar M. Saif
o.saif@hotmail.com; omar_sabry@cic-cairo.com

Mohamed Abouelatta
m.abouelatta@eng.asu.edu.eg

Abdelhalim Zekry
aaazekry@hotmail.com

Yasmine Elogail
yelogail@zewailcity.edu.eg

[1] Department of Electronics and Communications, Faculty of Engineering, Ain Shams University, Cairo 11566, Egypt

[2] Department of Communications and Electronics, Engineering School, Canadian International College (CIC), Giza, Egypt

[3] Engineering Physics and Mathematics Department, Faculty of Engineering, Ain Shams University, Cairo 11566, Egypt

[4] Nanotechnology and Nanoelectronics Engineering Department, UST at Zewail City, Giza 12578, Egypt

1 Introduction

Throughout numerous decades, crystalline silicon solar cells have been the prevailing technology in the PV industry due to its abundance, non-toxicity, and suitable energy bandgap [1, 2]. Recently, manufacturing thin-film Si cells with wafer's thickness less than 50 µm has been attempted. These cells offer substantial advantages concerning cost-competitiveness, flexibility, and ease of fabrication, using traditional methods similar to thick c-Si cells [3–5]. However, thin-film c-Si devices draw a poorer PCE (around 20%) than the traditional thick c-Si cells (which is greater than 26%) [4]. A potential approach to enhance the PCE of a PV cell involves creating a tandem cell configuration, using a wide-bandgap front cell positioned above the thin-film c-Si bottom cell. Given the silicon bandgap of 1.12 eV, the front cell materials require bandgap of (1.7–1.8) eV to current match both top and rear cells [6, 7]. Suitable wide-bandgap top cells for thin-film c-Si bottom cell that offer low-cost, flexibility,

high performance and stability have been a challenge. Over the past years, organic–inorganic metal halide perovskite PV cells occupied a remarkable consideration owing to their high PCEs and low-cost processes [8, 9]. Additionally, one attractive property for the perovskite material that makes it a promising material as a top sub-cell is its tunable bandgap (1.48 to 2.3 eV) [10, 11]. These properties make perovskites ideal candidates as wide-bandgap material for a tandem cell.

In a PVK/c-Si tandem, the top PVK and the rear Si sub-cells can be monolithically combined to produce 2-T tandem [12–14], or mechanically assembled, forming a four-terminal (4-T) tandem [15, 16]. In a 2T monolithic tandem, the front and back cells are linked in series, allowing their open-circuit voltages (V_{OC}) to add up. Nevertheless, the resultant short-circuit current (J_{SC}) is confined by the cell having the minor J_{SC}, leading to the requirement for current matching. Specifically, there are two common structures of heterojunction PVK/c-Si tandems depending on the structure of PVK cell design, either *n-i-p* PVK/c-Si or *p-i-n* PVK/c-Si [17–20]. In 2015, the first 2-T PVK/c-Si tandem cell has been published by Mailoa et al. [18], in which the front PVK cell was coupled to the c-Si homojunction bottom sub-cell by a Si tunnel junction. One year later, Albrecht et al. pioneered the utilization of a heterojunction Si-based PV cell as the rear sub-cell, leading to a series of PCE breakthroughs [17]. In 2017, Wu et al. presented developments in designing PVK/Si tandem solar cells that include a mesoscopic PVK front cell and a high-temperature Si-homojunction bottom cell. The Si-homojunction top and back surfaces were passivated by Al_2O_3/SiN_x and SiN_x films, respectively achieving an efficiency over 22% [21]. Later in 2018, Zheng J. demonstrated an efficiency of 21.8% on 16 cm^2 with $(FAPbI_3)_{0.83}(MAPbBr_3)_{0.17}$ as a top absorber which resulted in a higher V_{OC} [22]. Also, they developed an ARC layer that decreased optical losses and enhanced UV stability by utilizing a down-shifting material. The 2-T PVK/Si tandem solar cell was manufactured with an *n-i-p* structured PVK top cell and an n-Si homojunction back cell resulting in a PCE of approximately 23% [23]. Further, Yoon et al. achieved high-efficiency monolithic PVK/Si tandem cell by utilizing a sputtered high transparency and low resistivity ITO as a recombination layer, revealing a PCE of 25% [24]. In the middle of 2021, Chen et al. proposed a SnO_2-lithium chloride (LiCl) composite layer for a monolithic PVK/Si tandem solar cell. Such a tandem cell achieved an efficiency of 25.42% [25]. Recently, Ji Yeon Hyun et al. demonstrated a PVK/Si tandem SC based on a conventional Si homojunction structure utilizing a TOPcon to improve V_{OC}. They fabricated the device without the deposition of a recombination layer on a large area. The fabricated device demonstrated an efficiency of 17.3% and a V_{OC} of 1.784 V on 25 cm^2 active area [26]. In a recent development, researchers from Helmholtz-Zentrum Berlin (HZB) have accomplished a remarkable advancement in PV technology, setting a new world PCE record of 32.5% for a PVK/Si tandem, as officially accredited [27].

Most research endeavors have been directed towards the advancement of heterojunction-PVK/c-Si tandems, especially, the *p-i-n* PVK/c-Si tandem cells. On the other hand, some research has made great advances in developing the functioning of the *p-n* homojunction PVK single junction cell [28]. The first *p-n* homojunction PVK was realized by Danekamp et al. in 2018, utilizing the vacuum deposition of stoichiometrically tuned $MAPbI_3$ [29]. In the same line, Cui el al. designed a thin film PVK featuring a homojunction, combining *p*-type and *n*-type PVK layers, resulting in efficiencies of up to 21.38% [30]. However, the practical research is still going on in full swing to improve the performance of *p-n* homojunction PVK single-junction devices [28]. At present, studying the tandem cell that connects a wide-bandgap *p-n* homojunction PVK as a top cell with a bottom thin-film relatively narrow-bandgap cell can have a great attention. This comes from its relatively high V_{OC} due to the extra built-in electric field, low-manufacturing cost, and its flexibility. Thus, the integration of *p-n* homojunction PVK cell and a cheap c-Si thin-film cell can accomplish higher PCEs than single-junction cell. In addition to its higher efficiency, *p-n* homojunction PVK/thin-film Si tandem devices have the advantages of lightweight and flexibility that render them well for a wider variety of applications.

Notably, most of the previously aforementioned studies utilized Carrier Transport Layers (CTLs) in their structures due to their effective role in extracting and collecting photogenerated carriers. These layers include the Electron Transport Layer (ETL) and the Hole Transport Layer (HTL). The ETL collects and transports the electrons generated in the perovskite layer to the cathode, while the HTL transports the holes to the anode. However, CTLs may have drawbacks in some cases. One of these drawbacks is that ETL materials like TiO_2 generally require a high temperature annealing to attain good electrical characteristics which is not suitable for flexible cells [31, 32]. Moreover, some HTL materials like Spiro-OMeTAD have high prices which results in surging the cell cost [33]. Furthermore, ETL and HTL materials may have quite poor carrier mobilities, resulting in charge carrier transportation losses throughout the photogenerated carrier extraction mechanism [34]. Hence, to address these issues, simplifying the cell structure by excluding all the CTLs becomes necessary. Consequently, designing a high-efficient wide-bandgap *n-p* homojunction PVK omitting all CTLs as a front sub-cell, then combining this sub-cell to an optimized thin-film c-Si as a back sub-cell can boost the performance of a 2-T monolithic tandem cell. In this way, numerical simulations are used as an effective way for estimating the overall performance of *n-p* PVK/c-Si tandem cells and may be used to further identify the features of such

type of tandems. Till this moment, very little works studied tandems with a *p-n* homojunction PVK as a wide-bandgap front cell and/or utilizing c-Si thin-film rear cell [35–37].

This work proposes a 2-T monolithic tandem device connecting a *n-p* homojunction PVK (1.72 eV) as a top cell with a thin-film Si (1.12 eV) as a rear cell utilizing p^{++}/n^{++} Si tunnel junction between the two sub-cells. Employing all thin films can result in flexible tandems that may be exploited in different applications such as wearable devices. As a first step, to validate the Silvaco ATLAS simulator, the standalone heterojunction PVK and c-Si PV devices are calibrated against experimental studies, utilizing relevant geometrical and physical parameters. Next, the front sub-cell is designed, and the performance is compared using several structures: *n-p* hetero-homojunction (complete) PVK with CTLs, ETL-free *n-p* homojunction PVK, HTL-free *n-p* homojunction PVK, and CTL-free *n-p* homojunction PVK. Then, the design of the CTL-free *n-p* homojunction PVK is improved, and its performance is optimized employing different techniques. After boosting the performance of the thin-film Si cell, the optimized all-thin-film *n-p* PVK-homojunction/thin-film c-Si tandem is then simulated. Finally, the current-matching point (CMP) is examined. We believe that our optoelectronic simulation findings offer valuable insights into a promising technology that has the potential to serve as an alternative design, enhancing the PCE of tandem devices.

2 Simulation Approach and Device Arrangement

This section outlines the configuration of the initial all-thin-film *n-i-p* PVK/c-Si tandem cell. We commence by reviewing the fundamental physical models employed in the initial tandem solar cell design. Afterwards, we present calibrated thin-film structures for both the *n-i-p* PVK front sub-cell and the thin-film Si rear sub-cell, relying on experimental PV devices, along with their relevant factors. Finally, the construction of the initial tandem solar cell is complete.

2.1 TCAD Physical Modeling

Various software packages are available for examining the performance of solar cells, whether single-junction or tandems, including Silvaco [38], SCAPS [39], COMSOL [40], and wxAMPS [41]. In this study, all simulations are carried out by utilizing Silvaco Atlas device simulator. The electrical simulation involves applying the drift–diffusion model and solving Poisson's equation and continuity equations for both charge carriers (electrons and holes). Proper selection of physical models in Silvaco Atlas is crucial, and this work incorporates the physical models employed for designing the tandem structure. Considering the c-Si bottom cell, the Shockley–Read–Hall recombination model incorporating doping dependency (CONSRH) is activated. Additionally, Auger recombination is considered, particularly for regions with doping levels greater than 1×10^{18} cm^{-3} [42, 43]. To account for radiative recombination, the OPTR model is activated, even though its effect on practical Si-based cell performance is marginal. Bandgap narrowing effects are also included using the BGN model. Further, the mobility model incorporates the FLDMOB model for electric field dependence and the CONMOB model for concentration dependence, which is confirmed experimentally for Si and valid for a temperature of 300 K. Considering the *n-p* homojunction PVK cell, the SRH recombination is important due to observed recombination in this structure. Furthermore, Auger recombination (AUGER) is enabled to address recombination mechanisms in high-doped regions.

It is worth noting that the electrical connection between the two distinct cells of the tandem has two important aspects, (1) To create an ohmic contact and facilitate carrier extraction from neighboring cells with opposite polarities; and (2) to encourage the recombination of electrons and holes from these cells. This can be done by introducing a tunnel junction between the two cells or incorporating a recombination layer. This study introduces the interconnection between the two cells of the tandem utilizing the tunnel junction. To characterize the tunneling currents of the *p–n* junction, we employ the non-local band-to-band tunneling model (BBT.NONLOCAL) [38], which effectively accounts for the tunneling induced by the high doping in the tunnel diode.

2.2 Silvaco ATLAS Validation and Simulation Parameters

Here, we carry out a calibration process for the *n-i-p* PVK cell by modeling a thin-film configuration via the physical parameters accessible from literature [44]. The different layers of the initial *n-i-p* PVK structure, which is taken from an experimental work of [44], are shown in Fig. 1a. Basically, it consists of three main layers, the ETL, the PVK absorber, and the HTL. Experimentally, the intrinsic PVK (CsFAPbIBr) of 1.72 eV bandgap energy is sandwiched between a 40 nm thick *n*-type compact TiO_2 as an ETL and a 50 nm thick *p*-type Spiro-OMeTAD as an HTL to create a heterojunction PV cell. All previous cell technological parameters are captured from the fabricated PVK solar cell [44]. Other parameter values, including the doping concentration of each layer and various factors listed in Table 1, are derived from pertinent literature, as indicated in the table [38, 45–50]. In the simulation process, the work function of the FTO electrode is adjusted at 4.4 eV, whereas that of the back electrode (Au) is set to be 5.1 eV. In addition, the surface recombination velocity serves as a fitting parameter

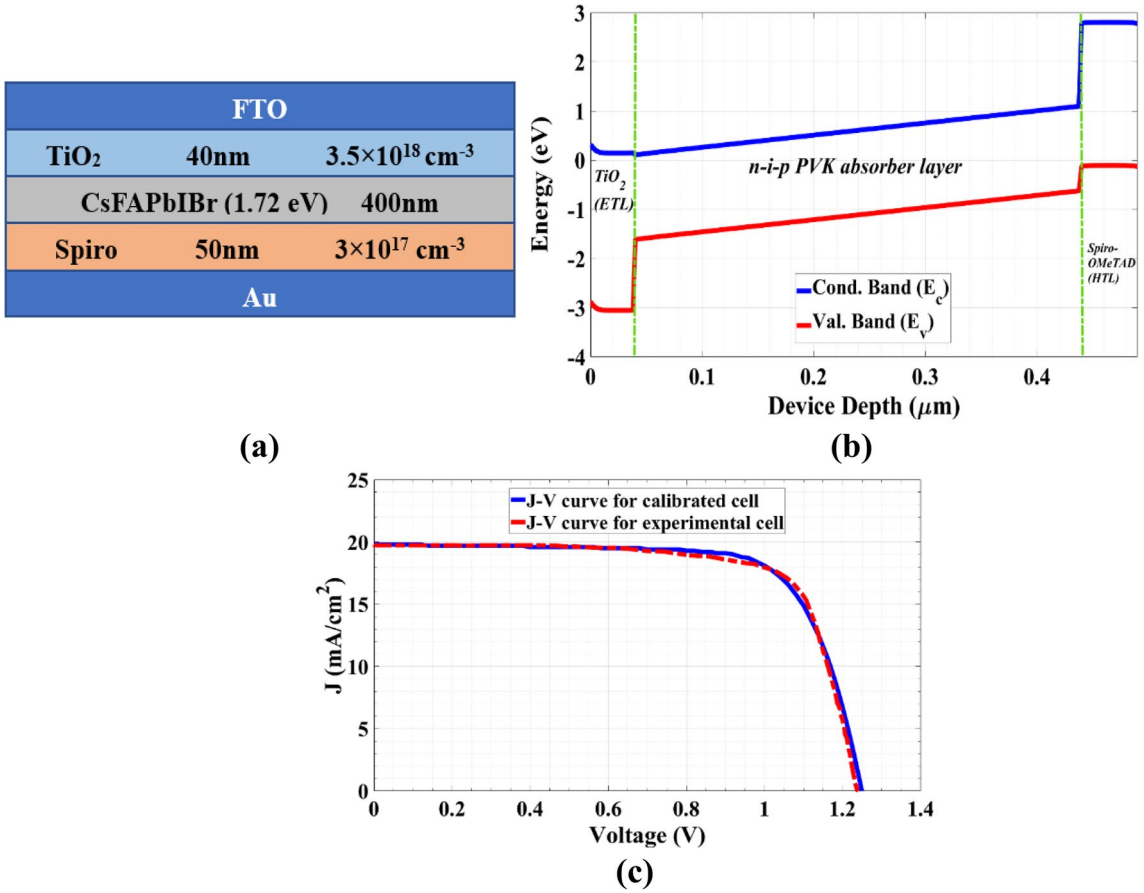

Fig. 1 **a** Main *n-i-p* perovskite structure involving design factors, **b** Energy band profile after contact at the dark condition, **c** *J-V* curves under AM1.5G illumination for both calibrated (Blue) and experimental (red) *n-i-p* PVK solar cells

Table 1 Parameter set of different materials utilized in the design of tandem cell

Parameter	TiO_2 [46, 49, 50]	PVK [45, 47]	Spiro-OMeTAD [46, 48]	c-Si [38]
Energy gap, E_g	3.2	1.72	2.91	1.12
Affinity, χ	3.95	4	2.32	4.05
Relative permittivity, ε_r	9	6.6	3	11.7
Electron mobility, μ_n	20	8.16	1×10^{-4}	Default Values of ATLAS
Hole mobility, μ_p	10	8	1×10^{-4}	
Cond. Band Effective DOS, N_C (cm^{-3})	1×10^{21}	2.2×10^{18}	2.2×10^{18}	2.8×10^{19}
Val. Band Effective DOS, N_V (cm^{-3})	2×10^{20}	1.9×10^{19}	1.9×10^{19}	1.04×10^{19}
Donor Concentration, N_D (cm^{-3})	3.5×10^{18}	-	-	Depending on Layer (Mentioned in the main paragraph)
Acceptor Concentration, N_A (cm^{-3})	-	1×10^{9}	3×10^{17}	

that differs according to the material quality. Notably, it primarily occurs at the interface between the PVK and the CTL. For our simulation, we utilize a surface recombination velocity of 1×10^4 cm/s for both the PVK/TiO_2 and PVK/Spiro-OMeTAD interfaces. As for the contacts' surfaces, the surface recombination velocity is set to 1×10^7 cm/s for both the TiO_2/FTO and Spiro-OMeTAD/Au interfaces.

Utilizing the previous specifications and the listed physical and geometrical parameters in Table 1, the energy band diagram, and the current density–voltage *(J-V)* characteristics are presented in Fig. 1b and c, respectively. Figure 1b demonstrates the band bending, indicating the emergence of the built-in potential in the active film in a manner that adequately separates electrons towards the ETL and holes

towards the HTL. Figure 1c depicts the *J-V* characteristics under the influence of AM1.5G illumination for the calibrated (simulated) structure along with the experimental structure. The calibrated cell records the following results, $J_{SC} = 19.79$ mA/cm^2, $V_{OC} = 1.249$ V, Fill Factor (FF) = 73.26%, and PCE = 18.106% that are in a decent match with the experimental results obtained from REF [44]. Table 2 demonstrates the match between the calibrated and experimental data, emphasizing the validation of the simulation model applied in the Atlas device simulator.

Conversely, the thin-film c-Si cell had been calibrated in our previous work [1]. The fabricated cell comprises three major layers, namely the emitter, base, and back surface field (BSF) films. The base thickness is 20 µm [4]. For precise calibration, various parameters, including doping densities and layer thicknesses of the emitter and BSF, are meticulously adjusted to ensure a nice fit between the simulated device performance and the experimental information. Specifically, the emitter, base, and BSF have doping concentrations of 5×10^{18} cm^{-3}, 5×10^{17} cm^{-3}, and 5×10^{18} cm^{-3}, respectively. Moreover, both the emitter and BSF layers have thicknesses of 100 nm and 1000 nm, respectively. Figure 2a introduces the cross-sectional schematic for the calibrated silicon solar cell showing the thicknesses and doping concentrations for each layer, while Fig. 2b depicts the energy band diagram of the calibrated silicon solar cell.

After executing ATLAS simulations, the performance parameters are extracted for the simulated thin-film c-Si cell, involving V_{OC}, J_{SC}, FF, and PCE. To validate the simulation results and the accuracy of the physical parameters, a comparison is made with the experimental values reported in [4] (Table 3). Further, the simulated illuminated *J-V* characteristics are plotted alongside the experimental results in Fig. 2. The good agreement between the simulation and measurements in Fig. 2c confirms the accuracy of the ATLAS simulator for calibrating this specific type of PV cell.

Table 2 TCAD results for the *n-i-p* PVK calibrated PV cell compared to experimental data

	V_{OC} [V]	J_{SC} [mA/cm^2]	*FF* [%]	*PCE* [%]
Experimental Results [44]	1.240	19.83	73.70	18.130
TCAD Calibration Results	1.249	19.79	73.26	18.106

Table 3 TCAD simulation results for the thin-film c-Si calibrated PV cell in comparison with experimental information

	V_{OC} [V]	J_{SC} [mA/cm^2]	*FF* [%]	*PCE* [%]
Experimental Results [4]	0.6180	35.30	78.30	17.300
TCAD Calibration Results	0.6142	34.86	82.40	17.416

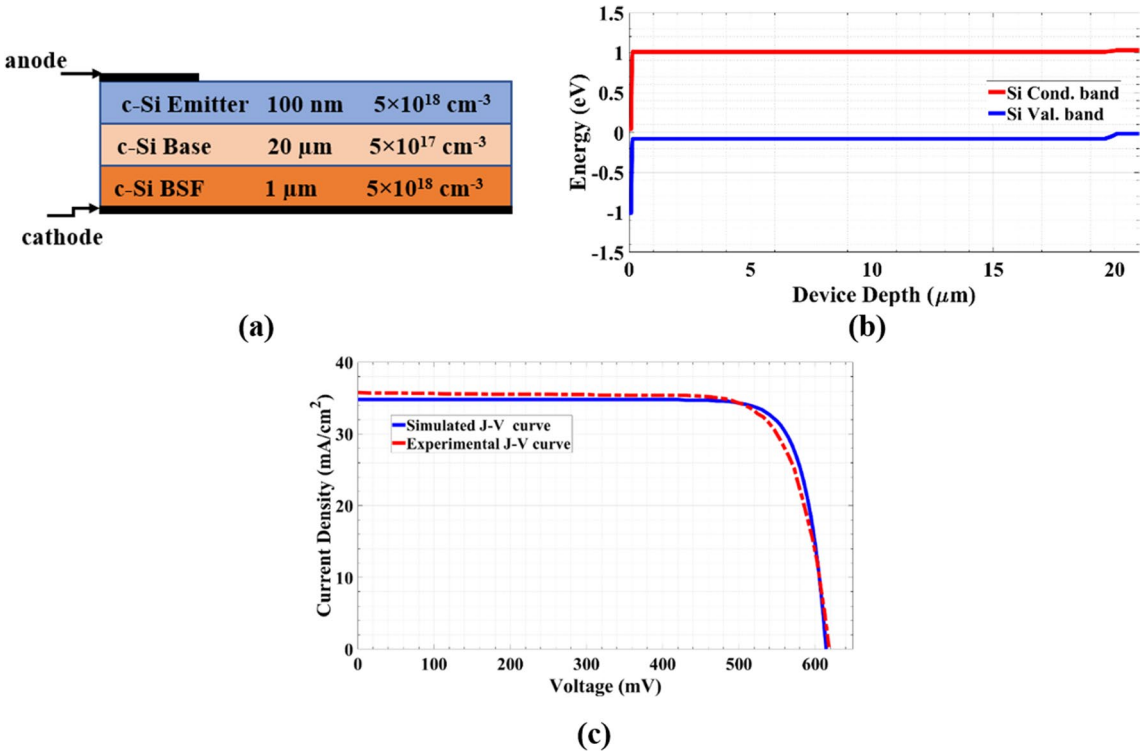

Fig. 2 (**a**) Structure of the calibrated c-Si solar cell, (**b**) Energy band diagram at dark condition, and (**c**) Experimental and simulated curves of the *J-V* under AM1.5G illumination

2.3 Initial *n-i-p* PVK/c-Si Device Structure

In this section, the previous two calibrated, *n-i-p* PVK cell and thin-film c-Si cell, are combined and connected to form an initial *n-i-p* PVK/c-Si tandem. The suggested configuration of the initial *n-i-p* PVK/c-Si is depicted in Fig. 3a indicating its design parameters. As mentioned earlier, the wide-bandgap *n-i-p* PVK is connected to the thin-film c-Si via p^{++}/n^{++} Si tunnel junction that acts as a recombination layer. From the electrical point of view and according to Kirchhoff's voltage law, the resultant V_{OC} is the summation of the separate V_{OC} for each cell. In addition, the current drawn by the tandem is coordinated by the lower current transported either through the front sub-cell or the back sub-cell. The initial tandem solar cell is simulated under spectrum of AM1.5G. Table 4 records the performance factors of the initial tandem, while Fig. 3b illustrates the illuminated *J-V* curves of the front, back, and tandem devices. As indicated in Table 4, the V_{OC} of the tandem equals the V_{OC} of the two sub-cells, while the total current is limited to the current drawn by front sub-cell leading to a PCE of 29.38%.

3 Results and Discussion

This section introduces, firstly, the impact of replacing the intrinsic PVK in *n-i-p* PVK single junction PV cell by an *n-p* homojunction PVK on the performance parameters of the single-junction cell. This is done by studying four different structures, complete hetero-homojunction cell, ETL-free *n-p* homojunction PVK cell, HTL-free *n-p* homojunction PVK cell, and CTL-free *n-p* PVK homojunction cell. Next, the performance of both standalone *n-p* homojunction PVK and thin-film c-Si cells are optimized. Accordingly, these optimized cells are connected to form the optimized all-thin-film *n-p* homojunction PVK/c-Si tandem device. Finally, the optimized cell is redesigned in order to achieve current-matching condition.

Table 4 Performance parameters for top PVK cell, rear thin-film Si cell, and initial PVK/c-Si tandem cell

	V_{OC} [V]	J_{SC} [mA/cm^2]	*FF* [%]	*PCE* [%]
Top n-i-p PVK cell	1.249	19.79	73.26	18.106
Bottom thin-film c-Si	0.614	34.86	82.40	17.416
Initial tandem cell	1.865	19.80	77.18	29.380

3.1 Design of *n-p* Homojunction PVK

In this subsection, the complete structure of FTO/TiO_2/*n-p* homojunction PVK/Spiro-OMeTAD/Au is designed and analyzed. In addition, the effect of omitting ETL, HTL, and both ETL and HTL is introduced.

Figure 4 shows the four different structures for *n-p* PVK-homojunction-based devices, complete structure (hetero-homojunction), ETL-free, HTL-free, and CTL-free *n-p* PVK-homojunction-based structures. The complete structure (Fig. 4a) is typical to that of Fig. 1a but replacing the intrinsic PVK layer by an *n-p* homojunction PVK. The total thickness of the homojunction PVK is kept being 400 nm. However, the ratio between the thickness of the *n*-type PVK and *p*-type PVK is determined to be as reported in [30, 51]. Furthermore, the minimum doping concentration for both *n*-type and *p*-type PVK should be higher than 1×10^{16} cm^{-3} in order to form an effective *p–n* junction [51]. Hence, a doping density of 5×10^{16} cm^{-3} is selected for *n*-type and *p*-type PVK. The used surface recombination at the interface between TiO_2/*n*-type PVK and *p*-type PVK/ SpiroOMeTAD is 1×10^{4} cm/s, while the surface recombination at contact/ETL and HTL/contact is 1×10^{7} cm/s.

As indicated in Fig. 5a, the *n-p* homojunction PVKs present an extra built-in electric field within the photoactive material, leading to the movement of holes towards the HTL and electrons towards the ETL. This additional field facilitates the efficient transport of the photo-excited current, resulting in reduced overall recombination rates

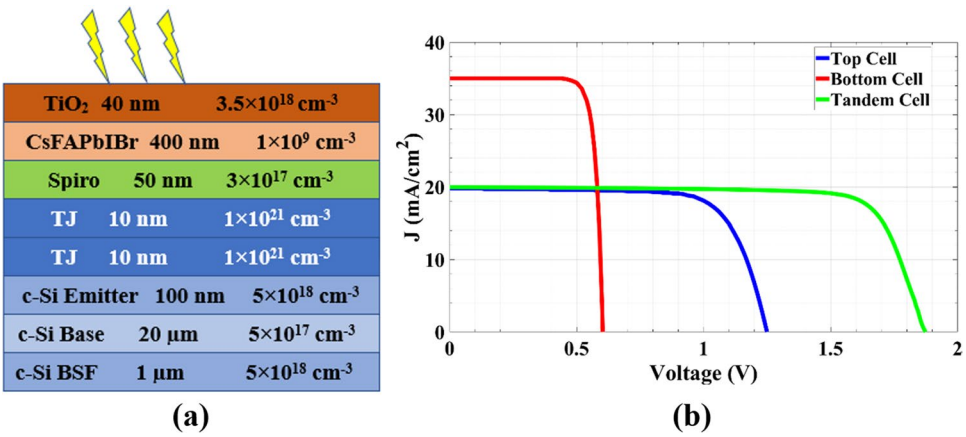

Fig. 3 **a** Schematic structure of the initial *n-i-p* PVK/c-Si tandem, and **b** *J-V* characteristic curves for top, rear, and tandem devices

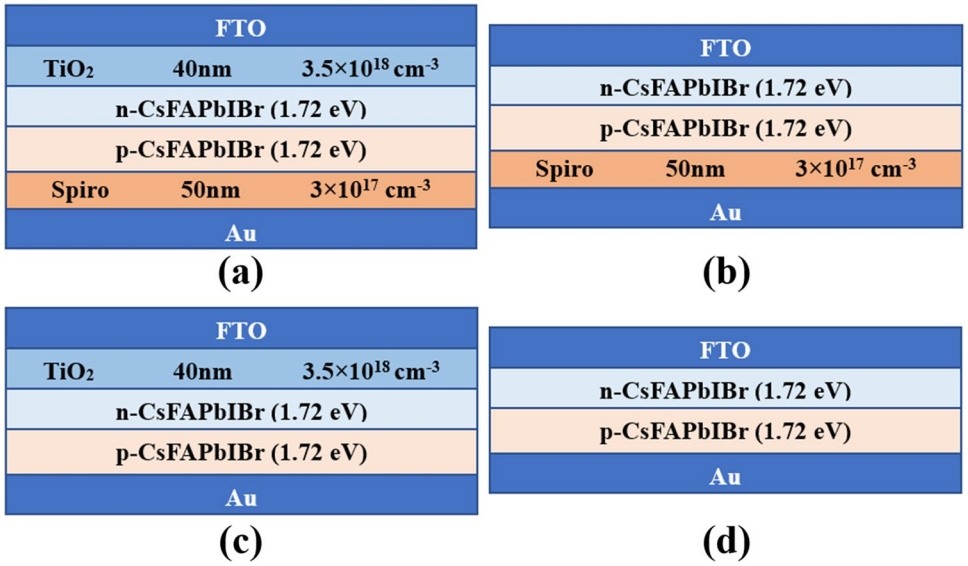

Fig. 4 Schematic structure for four different *n-p* PVK-homojunction-based single junction solar cell **a** hetero-homojunction (Complete) cell, **b** ETL-free cell, **c** HTL-free cell, and **d** CTL-free cell

(Fig. 5b), leading to an increase in J_{SC}. Figure 5c shows the energy band diagram for the *n-p* homojunction PVK cell along with the quasi-fermi levels for electron and hole for *n-p* homojunction PVK and *n-i-p* PVK cells. It is clear from the Fig. 5d that the difference of (E_{Fn}-E_{Fp}) for *n-p* homojunction PVK cell is marginally greater than that of the *n-i-p* PVK structure thanks to the induced electric field resulting in higher V_{OC} of the complete *n-p* homojunction PVK cell compared to that of the *n-i-p* PVK structure, causing enhanced PCE. A comparison between the performance parameters of *n-p* homojunction PVK and the intrinsic *n-i-p* PVK heterojunction cells is listed in Table 5. These performance parameters are plotted as *J-V* characteristics curves in Fig. 5e.

Figure 6 displays a comparative analysis of the performance of the aforementioned four structures to detect the limiting causes for the PCE. Figure 6a shows the external quantum efficiency (EQE) of the four different structures. Clearly, the CTL-Free cell generates the minimum J_{SC} as the lack of ETL and/or HTL cause severe surface recombination, while the spectral response of the ETL-free and CTL-free cells in very short wavelength range is greater than that of the complete structure and HTL-free cell because of the parasitic absorption losses in the ETL. As a result, omitting CTLs or one of them may hinder the J_{SC} as illustrated in Fig. 6b. The initial *n-p* homojunction PVK, ETL-free, HTL-free, and CTL-free cells exhibit J_{SC} of 19.93, 17.286, 17.438 and 13.746 mA/cm^2, respectively, resulting in PCEs of 20.77%, 12.97%, 15.88%, and 8.79%, respectively. As predictable, the initial *n-p* homojunction PVK cell demonstrates the best cell performance while the CTL-free cell exhibits the worst one. The performance parameters for each structure are summarized in Table 6.

Increasing carrier transport capabilities through the device can improve the performance of CTL-free cells. To enhance the carrier transportation, it is required to create an additional built-in electric field in the PVK film. As previously mentioned, the doping concentration is a key factor to create an efficient *n-p* junction. The higher doping concentration results in a greater electric field at the junction interface, leading to improved carrier transport and reduced recombination. This is favorable for increasing V_{OC}. Continuously increasing the doping concentration makes a very thinner width of the depletion layer of *n-p* junction resulting in a poor carrier extraction which is harmful to J_{SC}. In such a case, studying the effect of doping concentration in the performance of the CTL-Free cell is crucial. Furthermore, to boost the performance of the CTL-free cell, an increase in absorber thickness is essential to improve light absorption. In this way, the next section discusses different approaches for enhancing and increasing the functioning of CTL-free *n-p* homojunction PVK cell.

3.2 Design of High-Efficient CTL-Free *n-p* Homojunction PVK Cell

In this section, an enhancement to the performance of the CTL-Free *n-p* homojunction PVK solar cell is discussed. The surface recombination loss is one of the main limiting factors to PCE. So, introducing interlayers between the absorber and the contacts can reduce the surface recombination. Furthermore, studying the effect of doping concentration and the thickness of the absorber can be helpful to improve the performance of such cells. Thus, the performance enhancement of the CTL-Free *n-p* homojunction PVK solar cell is carried out in three independent steps,

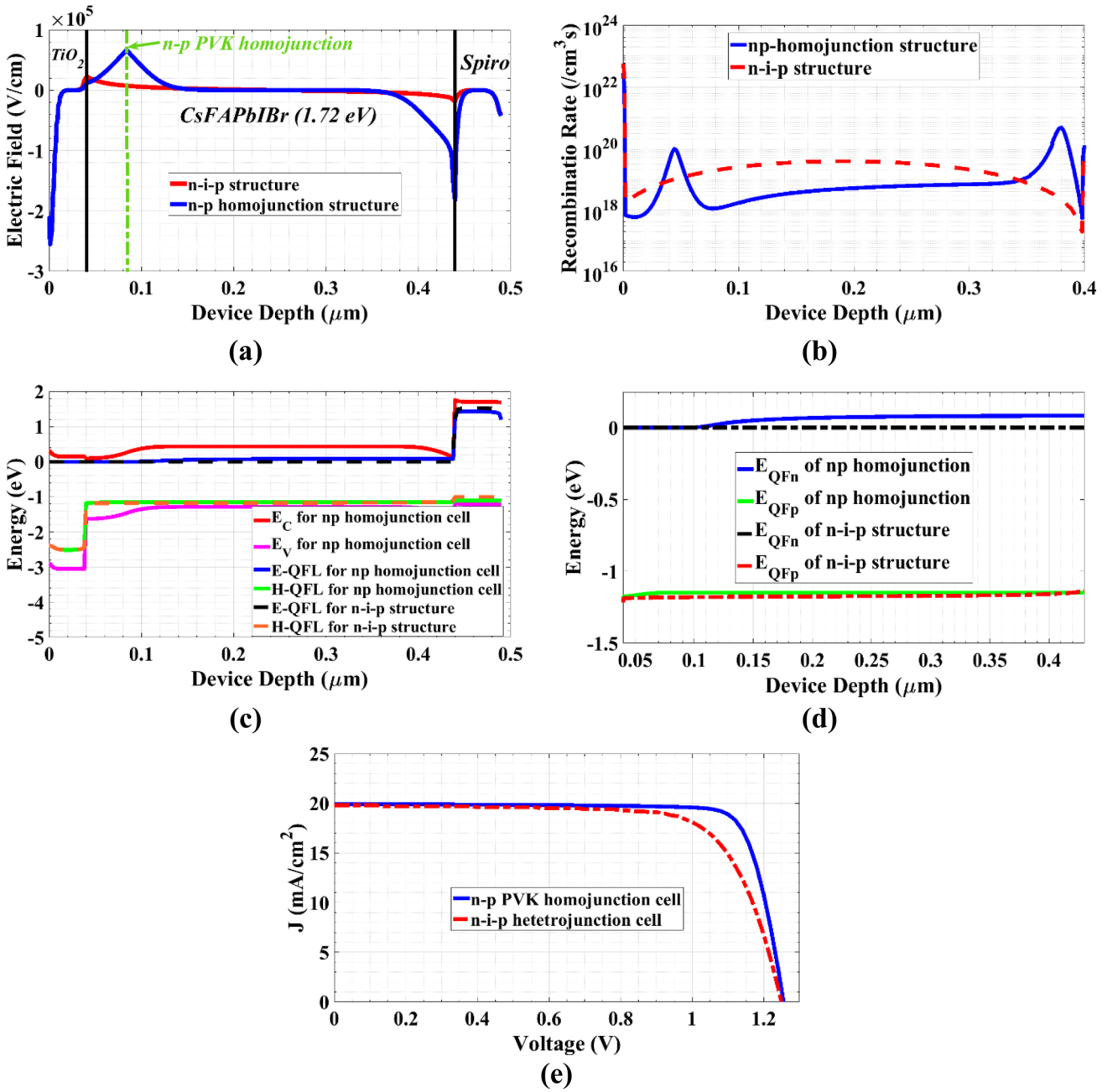

Fig. 5 **a** Electric Field Distribution, **b** Recombination rate throughout the device for both intrinsic (*n-i-p*) and hetero-homojunction (complete) structures, **c** Energy band diagram of complete *n-p* homojunction PVK cell along with the quasi-fermi level for both intrinsic (*n-i-p*) and hetero-homojunction (complete) structures, and **d** *J-V* characteristics curves for *n-p* homojunction PVK cell and intrinsic *n-i-p* PVK cell

Table 5 Performance parameters for *n-p* homojunction PVK cell and intrinsic *n-i-p* PVK cell

	V_{OC} [V]	J_{SC} [mA/cm^2]	*FF* [%]	*PCE* [%]
n-i-p PVK cell	1.249	19.79	73.26	18.106
n-p Homojunction PVK	1.256	19.93	83.08	20.770

applying front surface field (FSF) and BSF layers, optimizing the absorber thickness, and finally optimizing the doping concentration of the absorber.

3.2.1 Reduction of Surface Recombination

As previously mentioned, improving the performance of CTL-free cell can be accomplished by lowering the surface

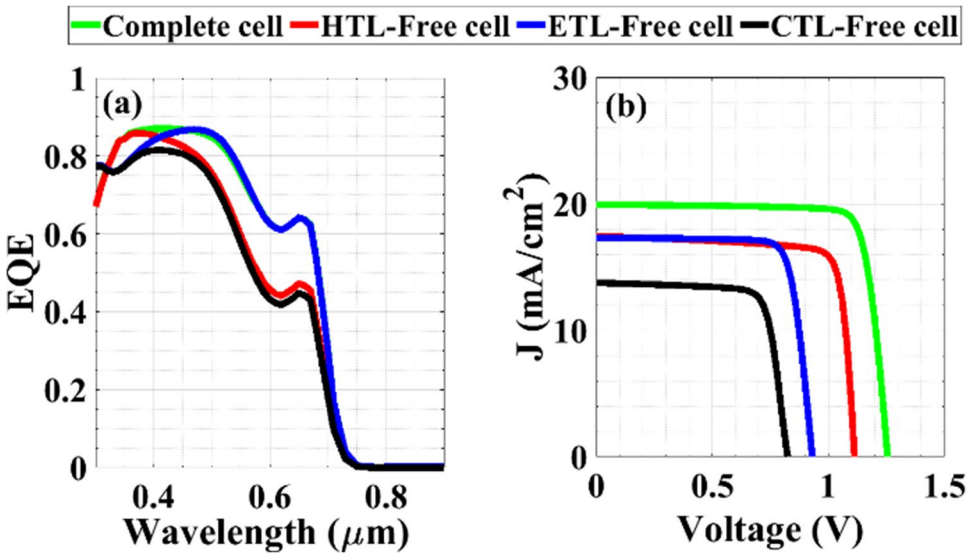

Fig. 6 **a** EQE, and **b** *J-V* characteristics, of four various structures of *n-p* homojunction PVK, initial, ETL-free, HTL-free, and CTL-free configurations

Table 6 A summary of the performance parameters for four different structure of *n-p* homojunction PVK cell

	V_{OC} [V]	J_{SC} [mA/cm^2]	*FF* [%]	*PCE* [%]
n-p Homojunction PVK	1.256	19.930	83.08	20.77
ETL-Free Cell	0.931	17.286	80.66	12.97
HTL-Free Cell	1.112	17.438	81.88	15.88
CTL-Free Cell	0.825	13.746	77.58	8.79

recombination losses between the PVK absorber and the contact. One method to alleviate the mechanism of the surface recombination arising at FTO/PVK and PVK/Au interfaces is designing the cell utilizing front surface field (FSF) and BSF films. The FSF and BSF films are made of perovskites that have a high doping density and a thin thickness. Based on the CTL-free structure in Fig. 4d, the design of an effective CTL-free *n-p* homojunction PVK cell is exhibited in Fig. 7a. The absorber layer thickness is kept being 400 nm. Following [51], The *n*-type emitter thickness is set at approximately 44 nm with a doping level of 5×10^{16} cm^{-3}, while the p-type base has a thickness of nearly 356 nm with a doping of 5×10^{16} cm^{-3}. Additionally, after an optimization process, the *n*-doped FSF and *p*-doped BSF are designed to have thicknesses of 5 nm and 50 nm, respectively, with a high doping density of 5×10^{19} cm^{-3} each.

The energy band profile in Fig. 7b illustrates the role of the FSF and BSF in the structure. The energy band diagram reveals a downward bending of the energy band with the FSF film and an upward bending with the BSF film, mainly due to the high doping impact. This implies that the FSF film enables the passage of electrons towards the contact and restricts the transfer of holes, while the BSF layer aids in hole migration towards the contact electrode and inhibits electron transport. This behavior is advantageous for enhancing charge collection, reducing surface recombination (as shown in Fig. 7c), and hence improving the PCE. Considering the electric field distribution, the field is shown to be significantly increased at the interfaces of FSF and BSF (Fig. 7d, the electric field distribution). This can significantly improve the functioning of CTL-free *n-p* homojunction PVK cell. As a result, the J_{SC} drawn by the structure with FSF and BSF is greater than that of the structure without FSF and BSF (Fig. 7e, J-V characteristics). The *n-p* homojunction PVK cell having both FSF and BSF films demonstrates the highest performance, where an efficiency of 19.704% is achieved, whereas the cells with no FSF and BSF exhibit the lowest performance, recording an efficiency of just 8.79%.

3.2.2 Effect of Absorber Thickness and Doping Density

The optimization of CTL-Free with FSF and BSF can be accomplished by increasing the absorber thickness to improve the light absorption. The thickness of the absorber is varied from 400 nm to 5 µm. As expected, the available photocurrent (APC) increases with widening the absorber layer thickness and gradually saturate at 3 µm (Fig. 8). Beyond an absorber thickness of 3 µm, the incremental increase in optical absorption becomes insignificant and can be disregarded. This reflects directly on the behavior of J_{SC} depending on the absorber thickness. Figure 9a shows that the J_{SC} rises when the absorber thickness increases to 3 µm. The change in J_{SC} after 3 µm is very small and can be neglected. Consequently, the PCE will be increased till 3µm-thick of absorber (Fig. 9b). Continuing to increase the absorber thickness has no PCE enhancement but does

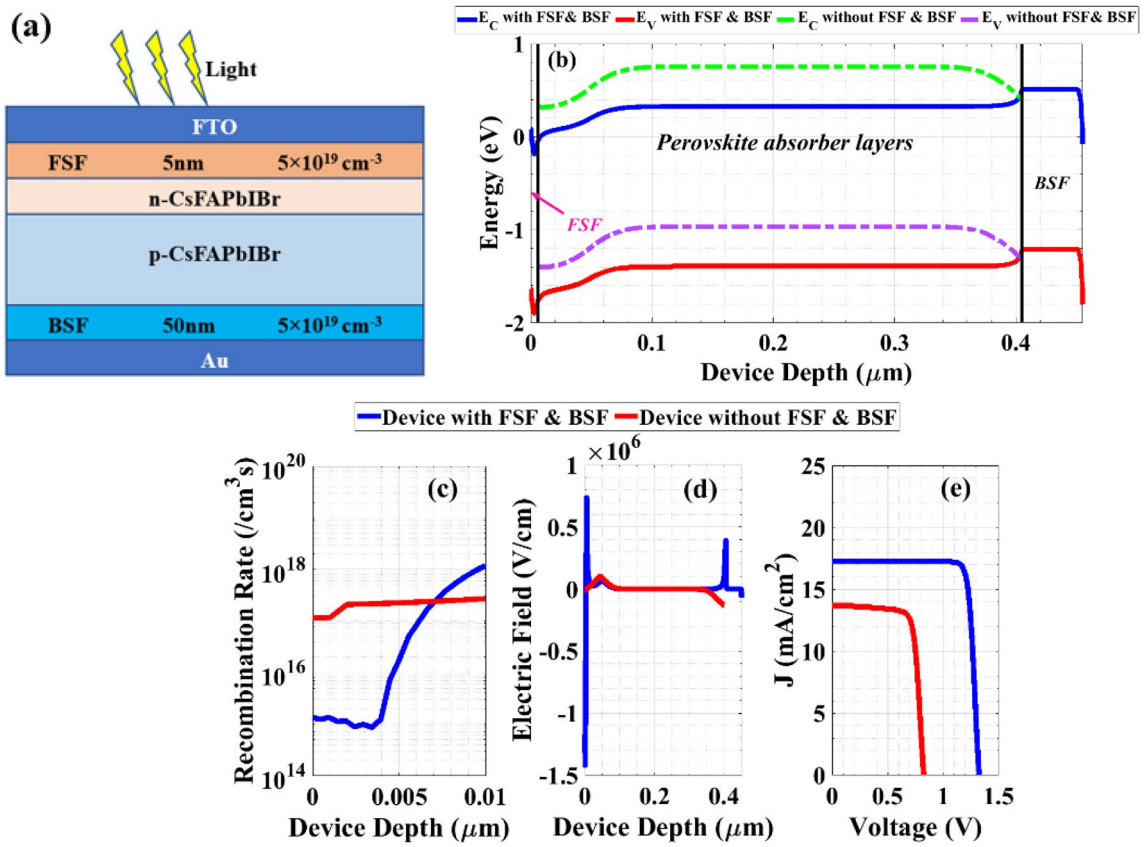

Fig. 7 **a** Schematic of efficient *n-p* homojunction PVK with FSF and BSF, **b** Energy band diagram of the *n-p* homojunction PVK with FSF and BSF, **c** Surface recombination for the device with and without FSF and BSF, **d** Electric Field Distribution for both devices, and **e** *J-V* characteristics curves for both devices

reduce the Fill Factor marginally, resulting in inferior cell performance. So, we select 3 µm to be the optimum absorber thickness.

Moreover, the doping concentrations of both types of the absorber have a direct influence on improving the carrier transportation through the *n-p* junction and hence refining the performance of the CTL-free homojunction PVK with FSF and BSF. On the other hand, the high doping concentrations make the depletion region of the *n-p* junction narrower, resulting in a wider quasi-neutral region. In this context, the carrier moves by diffusion process, that leads to a weak carrier extraction, which is harmful to J_{SC}. In our simulation, the doping density of both *n*-type PVK and *p*-type PVK layers are varied from 5×10^{16} /cm^3 to 5×10^{19} /cm^3. Studying the dependency of the PCE on the doping concentrations of PVK is introduced in Fig. 10. It is clear that the PCE has its peak value (24.09%) at *n*-type doping and *p*-type doping of 1×10^{17} /cm^3 and 7×10^{17} /cm^3, respectively.

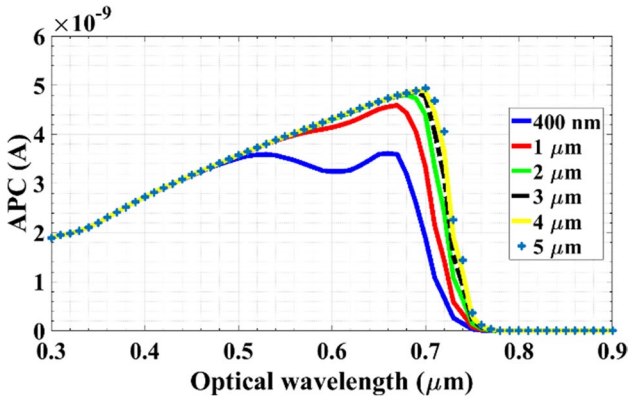

Fig. 8 The available photocurrent of CTL-Free *n-p* homojunction PVK with FSF and BSF at different absorber thickness

The proposed structure of *n-p* homojunction PVK solar cell utilized FSF and BSF layer with doping concentrations of 5×10^{19} /cm^3 and thicknesses of 5 nm and 50 nm respectively, the total (sum) thickness of the two PVK layers is selected to be 3 µm where the *n*-type layer share about 1:9 ratio of the total absorber thickness. Finally, the doping concentration for such layers are 1×10^{17} /cm^3 and 7×10^{17} /cm^3 for *n*-type and *p*-type PVK. Table 7 summarizes the performance parameters of the proposed PV cell in three

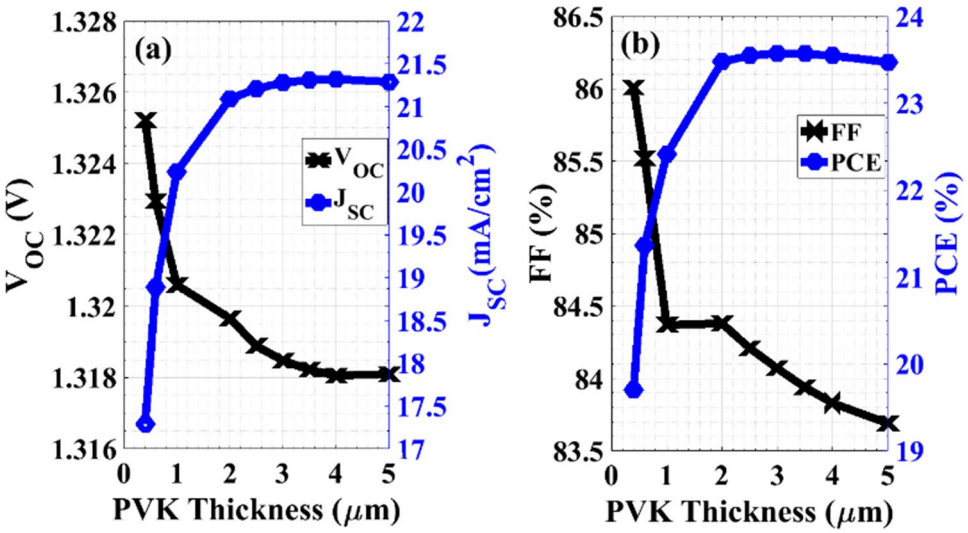

Fig. 9 Performance parameters of CTL-Free *n-p* Homojunction PVK with FSF and BSF when altering the absorber thickness (**a**) J_{SC} and V_{OC}, and (**b**) FF and PCE

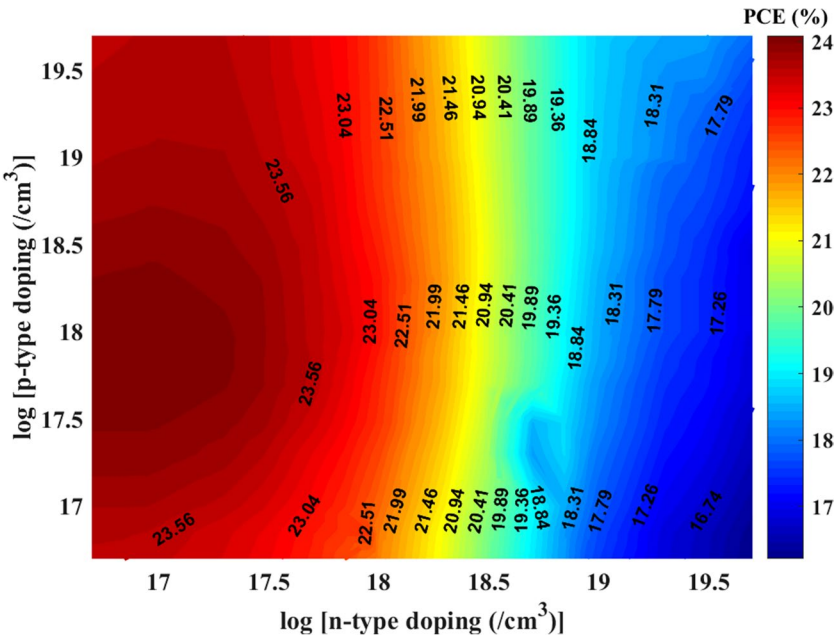

Fig. 10 Contour map for the dependency of the PCE of the proposed PVK single-junction on the doping concentration of *n*-type and *p*-type PVK absorber

Table 7 Performance parameters of the proposed n-p Homojunction PVK cell compared to the CTL-free Cell

	V_{OC} [V]	J_{SC} [mA/cm^2]	*FF* [%]	*PCE* [%]
CTL-Free Cell	0.825	13.746	77.58	8.790
Applying FSF & BSF	1.326	17.294	86.00	19.704
Optimizing Absorber thickness	1.318	21.276	84.07	23.573
Optimizing absorber doping conc	1.338	21.020	85.65	24.090

steps. First, utilizing FSF and BSF, second, optimizing the absorber thickness, and finally optimizing the doping concentration of *n*-type and *p*-type absorbers. The *J-V* and EQE characteristics of the proposed *n-p* homojunction PVK cell are displayed in Fig. 11. The proposed single PVK cell presents an improvement in the light absorption, especially, at the range of higher wavelength. This leads to higher J_{SC}. Also, the proposed cell implies a high V_{OC} thanks to the optimized doping concentration that makes a strong built-in field.

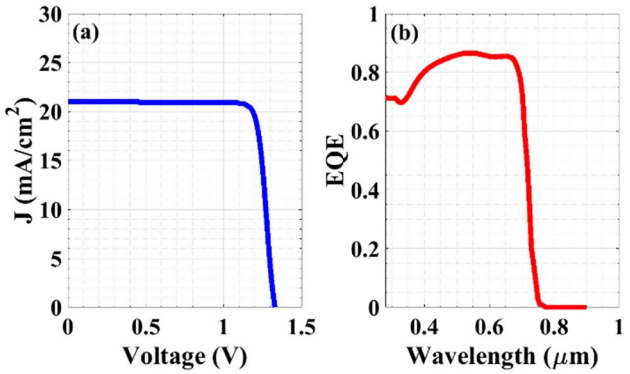

Fig. 11 **a** *J-V* characteristics curves, and **b** EQE of the proposed *n-p* homojunction PVK solar cell

3.3 Design of High-Efficient Standalone Thin-Film c-Si Solar Cell

In this section, an optimization technique to boost the performance of thin-film Si single junction cell is presented. The optimization technique follows three steps: (i) variation of emitter doping (ii) changing the base doping and (iii) changing the BSF doping (Fig. 12). The emitter is designed to have a high doping concentration. The doping level of the emitter is changed from 1×10^{18} /cm^3 to 1×10^{21} /cm^3. The maximum achievable PCE happens at a doping value of 1×10^{21} /cm^3 for the emitter, after which the PCE starts to degrade. On the other hand, the base doping concentration is optimized when varying from 1×10^{16} /cm^3 to 1×10^{20} /cm^3 while keeping the emitter doping concentration constant at 1×10^{20} /cm^3. The maximum PCE is recorded to be greater than 20% at doping of 1×10^{16} /cm^3.

Furthermore, the BSF film, heavily doped at the bottom side of the cell, acts as a barrier hindering the flow of minority carriers toward the back contact. For low doping concentrations, the electric field at the interface is ineffective, leading to reduced collection efficiency of photo carriers at the contact. Conversely, increasing the doping level in the BSF film leads to a greater electric field at the interface. Consequently, the barrier for minority carrier transfer toward the back region is enhanced. This reduction in surface recombination results in higher values of V_{OC} and J_{SC}, thereby the PCE of thin-film Si cell is optimized. Here, the BSF doping level is varied in the range 1×10^{18} /cm^3—1×10^{21} /cm^3 while keeping the emitter and base doping densities constant at 1×10^{20} /cm^3 and 1×10^{16} /cm^3, respectively. The doping density of the BSF is optimized at 1×10^{20} /cm^3. Beyond this level, the performance of the optimized Si cell is saturated. The *J-V* curve as well as the EQE spectrum of the optimized thin-film Si cell is portrayed in Fig. 13. Table 8 lists the performance metrics of the optimized thin-film Si single junction device.

3.4 Design of All-Thin-Film PVK/c-Si Tandem Cell

Here, we propose an all-thin-film PVK/c-Si tandem cell utilizing the previously optimized standalone wide-band *n-p*

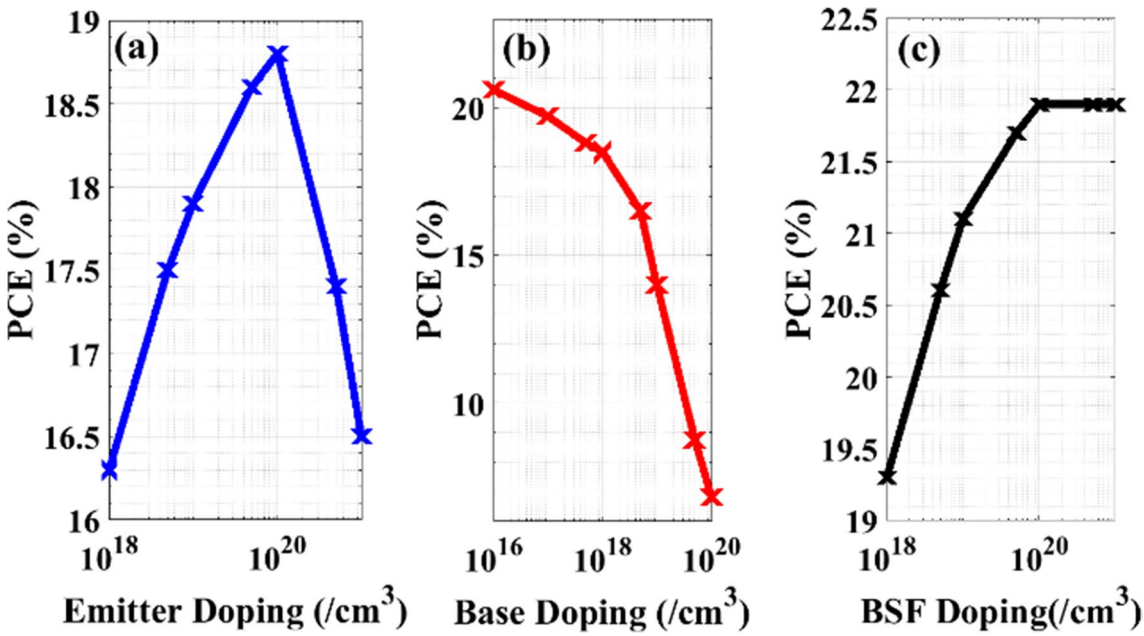

Fig. 12 PCE dependency on (**a**) Emitter doping concentration, (**b**) base doping density, and (**c**) BSF doping concentration for the thin-film Si single junction cell

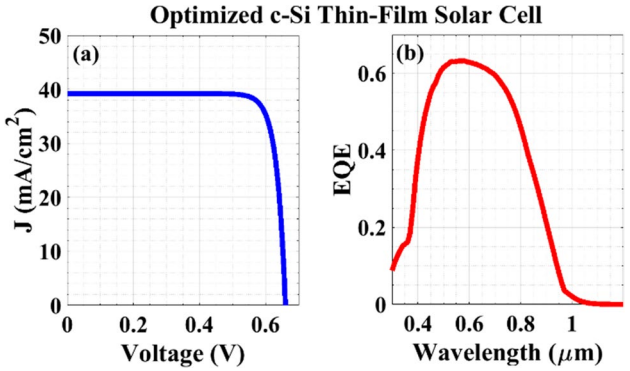

Fig. 13 **a** *J-V* characteristics curve, and **b** EQE of optimized thin-film c-Si solar cell

Table 8 Performance metrics of the thin-film c-Si solar cell

	V_{OC} [V]	J_{SC} [mA/cm^2]	*FF* [%]	*PCE* [%]
Optimized thin-film c-Si	0.66	39.21	83.86	21.71

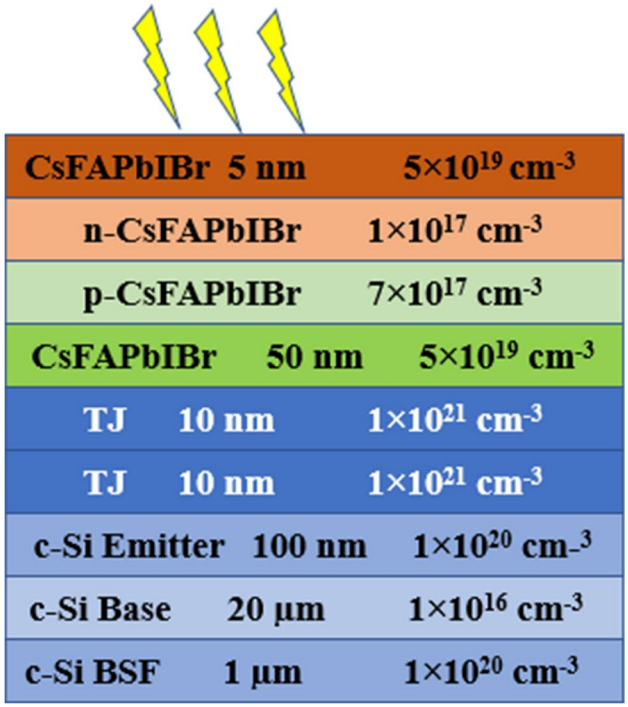

Fig. 14 Schematic structure of the all-thin-film PVK/c-Si tandem cell

homojunction PVK cell as a front sub-cell and the optimized thin-film c-Si as a rear sub-cell. Both top and rear sub-cells are attached using the p^{++}/n^{++} Si tunnel diode. The tunnel diode must not absorb any portion of the incident solar irradiation spectrum. This is achieved by fulfilling two design specifications: first, ensuring the diode is heavily doped, and second, making both the n-region and p-region of the diode very thin (few nanometers) [52]. A schematic of the optimized tandem device is established in Fig. 14. The *n-p* homojunction PVK/c-Si thin film tandem records the following performance parameters, $V_{OC}=1.99$ V, $J_{SC}=21$ mA/cm^2, $FF=90.17\%$, and PCE$=37.68\%$. Figure 15 depicts the *J-V* curves and EQE spectra for the front cell, bottom cell, and tandem cell. Clearly, the V_{OC} of the tandem is the summation of both V_{OC} of the top and rear cells, while the current is limited by the current drawn by the top cell as it is the minimum current (Fig. 15a). Furthermore, Fig. 15b shows the simulated EQE of the all-thin-film PVK/c-Si tandem cell. Notably, the top *n-p* PVK cell absorbs photon of lower wavelength range while the bottom cell absorbs photon of higher energy. These illustrate the effectiveness of the tunnel diode utilized for connecting both top and rear cells.

Moreover, to comprehend the CMP, the front absorber thickness is varied from 400 nm to 5 µm, keeping the bottom absorber thickness constant at 20 µm and changing the thickness of its emitter to 800 nm and the BSF layer thickness to 500 nm. Figure 16a displays the variation in J_{SC} of the front and bottom devices against the thickness of the front absorber, indicating considerable dependence of the top absorber thickness. As the top absorber thickness widens, the J_{SC} of the front sub-cell improves while it decreases at the rear sub-cell. The reason behind this trend is that with increasing thickness of the top absorber, more photons are absorbed, leading to less light being transmitted to the rear sub-cell. A CMP occurs at $J_{SC}=20.9$ mA/cm^2 and is satisfied top absorber thickness of 2.18 µm. Under this condition, the performance of the all-thin-film *n-p* homojunction PVK/c-Si tandem is simulated where the corresponding *J-V* characteristics of front, rear, and tandem PV cells are illustrated in Fig. 16b. Again, the value of V_{OC} of the tandem equals 1.95 V, approximately, the sum of those of top (1.321 V) and bottom (0.622 V) cells, resulting in an efficiency of 36.37%.

Finally, a comparison between our optimized proposed 2-T monolithic all-thin-film tandem cell and other tandem structures is provided as given in Table 9. Some of the highlighted tandems are based on experimental studies, whereas others are obtained through numerical simulations. All studied of PVK/c-Si are based on *n-i-p* PVK structure instead of *n-p* homojunction PVK. The results indicate the great effectiveness of utilizing the *n-p*-homojunction PVK based tandems.

4 Conclusion

In this simulation work, we introduced a 2-T monolithic all-thin-film PVK/c-Si tandem design. The top sub-cell involves a wide-band *n-p* homojunction PVK cell having a bandgap

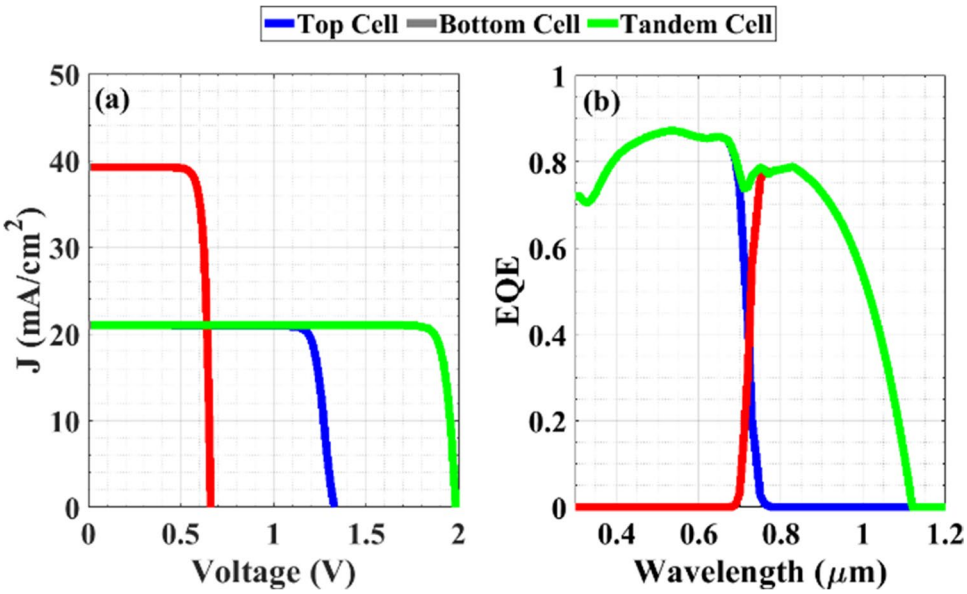

Fig. 15 **a** *J-V* characteristics curve, and **b** EQE, for the optimized top sub-cell, bottom sub-cell, and tandem cell

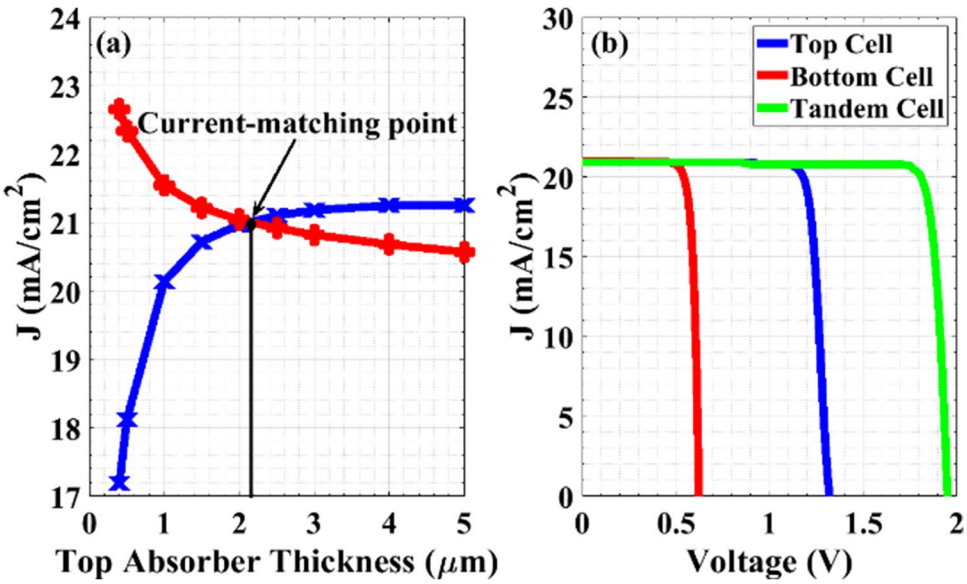

Fig. 16 **a** J_{SC} of the front sub-cell and bottom sub-cell versus the top absorber thickness, and **b** *J-V* curves for top, back, and tandem cells at current matching condition

Table 9 Comparative analysis of selected tandem solar cells, including different experimental and simulation studies

Structure	Method	V_{OC} [V]	J_{SC} [mA/cm^2]	*FF* [%]	*PCE* [%]	Ref
2-T n-i-p PVK/Si	Exp	1.65	11.5	75	13.7	[18]
2-T p-i-n PVK/Si	Exp	1.78	14	79.5	18.1	[17]
4-T n-i-p PVK/Si	Exp	1.808	-	-	29.65	[15]
2-T PVK/Si	Exp	1.57	16.54	75.14	19.38	[20]
2-T PVK/Si	Exp	1.98	20.24	81.2	32.5	[27]
2-T PVK/Si	Sim	1.76	16.01	86.7	24.4	[53]
2-T PVK/Si	Sim	2.01	18.81	83.61	31.67	[54]
2-T *p-n* PVK/CIGS	Sim	2.25	25.8	73.02	30.71	[37]
2-T *n-p* homojunction PVK/c-Si	Sim	1.95	20.9	89.33	36.37	This Study

of 1.72 eV, while the rear cell is based on c-Si whose bandgap is 1.12 eV. To validate the performance of both standalone sub-cells, we calibrated the *n-i-p* PVK cell and the c-Si cell against experimental data. Then, we investigated the impact of the *n-p* homojunction PVK through four different configurations, highlighting the significance of replacing the heterojunction PVK layer with the *n-p* homojunction PVK layer. The optimization process involves studying the dependency of the performance of the *n-p* homojunction PVK cell on the absorber layer thickness, absorber layer doping concentration as well as optimizing the bottom c-Si cell. Upon designing the PVK/c-Si tandem device to meet the CMP, we achieved remarkable results, including a high V_{OC} of 1.95 V and a high efficiency of 36.37%. These results indicate significant progress compared to the initial design that utilized an *n-i-p* PVK. The success of this study opens up possibilities for flexible, and highly efficient perovskite tandem devices.

Authors' Contributions Omar M. Saif, Ahmed Shaker, and Yasmine Elogail wrote the original draft, reviewing & editing the main manuscript text. Omar M. Saif and Ahmed Shaker performed the simulation and prepared the figures. Abdelhalim Zekry and Mohamed Abouelatta supervised the work. All authors shared conceptualization, methodology, and validation. All authors reviewed the manuscript.

Funding Open access funding provided by The Science, Technology & Innovation Funding Authority (STDF) in cooperation with The Egyptian Knowledge Bank (EKB).

Data Availability Data will be made available on reasonable request.

Declarations

Ethical Approval Not Applicable.

Consent to Participate Not Applicable.

Consent for Publication Not Applicable.

Competing Interests The authors declare no competing interests.

References

1. Saif OM, Zekry A, Shaker A, Abouelatta M, Alanazi TI, Saeed A (2023) Design and Optimization of a Self-Protected Thin Film c-Si Solar Cell against Reverse Bias. Materials 16:2511. https://doi.org/10.3390/ma16062511
2. Okil M, Salem MS, Abdolkader TM, Shaker A (2022) From Crystalline to Low-cost Silicon-based Solar Cells: a Review. Silicon 14:1895–1911. https://doi.org/10.1007/s12633-021-01032-4
3. Yamamoto K, Nakajima A, Yoshimi M, Sawada T, Fukuda S, Suezaki T, Ichikawa M, Koi Y, Goto M, Meguro T, Matsuda T, Kondo M, Sasaki T, Tawada Y (2004) A high efficiency thin film silicon solar cell and module. Sol Energy 77:939–949. https://doi.org/10.1016/j.solener.2004.08.028
4. Hwang I, Jeong Y, Shiratori Y, Park J, Miyajima S, Yoon I, Seo K (2020) Effective Photon Management of Non-Surface-Textured Flexible Thin Crystalline Silicon Solar Cells. Cell Rep Phys Sci 1:100242. https://doi.org/10.1016/j.xcrp.2020.100242
5. Hwang I, Um H-D, Kim B-S, Wober M, Seo K (2018) Flexible crystalline silicon radial junction photovoltaics with vertically aligned tapered microwires, Energy. Environ Sci 11:641–647. https://doi.org/10.1039/C7EE03340K
6. Jaysankar M, Raul BAL, Bastos J, Burgess C, Weijtens C, Creatore M, Aernouts T, Kuang Y, Gehlhaar R, Hadipour A, Poortmans J (2019) Minimizing Voltage Loss in Wide-Bandgap Perovskites for Tandem Solar Cells. ACS Energy Lett 4:259–264. https://doi.org/10.1021/acsenergylett.8b02179
7. McMeekin DP, Sadoughi G, Rehman W, Eperon GE, Saliba M, Hörantner MT, Haghighirad A, Sakai N, Korte L, Rech B, Johnston MB, Herz LM, Snaith HJ (1979) A mixed-cation lead mixed-halide perovskite absorber for tandem solar cells. Science 351(2016):151–155. https://doi.org/10.1126/science.aad5845
8. Saif OM, Zekry AH, Abouelatta M, Shaker A (2023) A Comprehensive Review of Tandem Solar Cells Integrated on Silicon Substrate: III/V vs Perovskite. Silicon. https://doi.org/10.1007/s12633-023-02466-8
9. Green MA, Ho-Baillie A, Snaith HJ (2014) The emergence of perovskite solar cells. Nat Photonics 8:506–514. https://doi.org/10.1038/nphoton.2014.134
10. Docampo P, Bein T (2016) A Long-Term View on Perovskite Optoelectronics. Acc Chem Res 49:339–346. https://doi.org/10.1021/acs.accounts.5b00465
11. Gao P, Grätzel M, Nazeeruddin MK (2014) Organohalide lead perovskites for photovoltaic applications. Energy Environ Sci 7:2448–2463. https://doi.org/10.1039/C4EE00942H
12. Köhnen E, Wagner P, Lang F, Cruz A, Li B, Roß M, Jošt M, Morales-Vilches AB, Topič M, Stolterfoht M, Neher D, Korte L, Rech B, Schlatmann R, Stannowski B, Albrecht S (2021) 27.9% efficient monolithic perovskite/silicon tandem solar cells on industry compatible bottom cells. Solar RRL 5:2100244. https://doi.org/10.1002/solr.202100244
13. Zhu S, Hou F, Huang W, Yao X, Shi B, Ren Q, Chen J, Yan L, An S, Zhou Z, Ren H, Wei C, Huang Q, Li Y, Hou G, Chen X, Ding Y, Wang G, Li B, Zhao Y, Zhang X (2018) Solvent Engineering to Balance Light Absorbance and Transmittance in Perovskite for Tandem Solar Cells. Solar RRL 2:1800176. https://doi.org/10.1002/solr.201800176
14. Wang S, Wang P, Chen B, Li R, Ren N, Li Y, Shi B, Huang Q, Zhao Y, Grätzel M, Zhang X (2022) Suppressed recombination for monolithic inorganic perovskite/silicon tandem solar cells with an approximate efficiency of 23%. EScience 2:339–346. https://doi.org/10.1016/j.esci.2022.04.001

15. Abbasiyan A, Noori M, Baghban H (2022) A highly efficient 4-terminal perovskite/silicon tandem solar cells using QIBC and IBC configurations in the top and bottom cells, respectively. Mater Today Energy 28:101055. https://doi.org/10.1016/j.mtener.2022.101055
16. Rohatgi A, Zhu K, Tong J, Kim DH, Reichmanis E, Rounsaville B, Prakash V, Ok Y-W (2020) 26.7% Efficient 4-terminal perovskite-silicon tandem solar cell composed of a high-performance semi-transparent perovskite cell and a doped Poly-Si/SiO x passivating contact silicon cell. IEEE J Photovolt. 10:417–422. https://doi.org/10.1109/JPHOTOV.2019.2963564
17. Albrecht S, Saliba M, Correa Baena JP, Lang F, Kegelmann L, Mews M, Steier L, Abate A, Rappich J, Korte L, Schlatmann R, Nazeeruddin MK, Hagfeldt A, Grätzel M, Rech B (2016) Monolithic perovskite/silicon-heterojunction tandem solar cells processed at low temperature. Energy Environ Sci. 9:81–88. https://doi.org/10.1039/C5EE02965A
18. Mailoa JP, Bailie CD, Johlin EC, Hoke ET, Akey AJ, Nguyen WH, McGehee MD, Buonassisi T (2015) A 2-terminal perovskite/silicon multijunction solar cell enabled by a silicon tunnel junction. Appl Phys Lett 106:121105. https://doi.org/10.1063/1.4914179
19. Bush KA, Manzoor S, Frohna K, Yu ZJ, Raiford JA, Palmstrom AF, Wang H-P, Prasanna R, Bent SF, Holman ZC, McGehee MD (2018) Minimizing Current and Voltage Losses to Reach 25% Efficient Monolithic Two-Terminal Perovskite-Silicon Tandem Solar Cells. ACS Energy Lett 3:2173–2180. https://doi.org/10.1021/acsenergylett.8b01201
20. Zhang J, Lu L, Zhang J, Li S, Hua X, Zhu X, Ding Y-A, Lin Y, Zhang S-T, Li D (2023) Monolithic perovskite/silicon tandem solar cells with optimized front zinc doped indium oxides and industrial textured silicon heterojunction solar cells. J Alloys Compd 932:167640. https://doi.org/10.1016/j.jallcom.2022.167640
21. Wu Y, Yan D, Peng J, Duong T, Wan Y, Phang SP, Shen H, Wu N, Barugkin C, Fu X, Surve S, Grant D, Walter D, White TP, Catchpole KR, Weber KJ (2017) Monolithic perovskite/silicon-homojunction tandem solar cell with over 22% efficiency. Energy Environ Sci 10:2472–2479. https://doi.org/10.1039/C7EE02288C
22. Zheng J, Mehrvarz H, Ma F-J, Lau CFJ, Green MA, Huang S, Ho-Baillie AWY (2018) 21.8% Efficient Monolithic Perovskite/Homo-Junction-Silicon Tandem Solar Cell on 16 cm 2. ACS Energy Lett. 3:2299–2300. https://doi.org/10.1021/acsenergylett.8b01382
23. Zheng J, Mehrvarz H, Liao C, Bing J, Cui X, Li Y, Gonçales VR, Lau CFJ, Lee DS, Li Y, Zhang M, Kim J, Cho Y, Caro LG, Tang S, Chen C, Huang S, Ho-Baillie AWY (2019) Large-Area 23%-Efficient Monolithic Perovskite/Homojunction-Silicon Tandem Solar Cell with Enhanced UV Stability Using Down-Shifting Material. ACS Energy Lett 4:2623–2631. https://doi.org/10.1021/acsenergylett.9b01783
24. Yoon W, Scheiman D, Ok Y-W, Song Z, Chen C, Jernigan G, Rohatgi A, Yan Y, Jenkins P (2020) Sputtered indium tin oxide as a recombination layer formed on the tunnel oxide/poly-Si passivating contact enabling the potential of efficient monolithic perovskite/Si tandem solar cells. Sol Energy Mater Sol Cells 210:110482. https://doi.org/10.1016/j.solmat.2020.110482
25. Chen B, Wang P, Li R, Ren N, Chen Y, Han W, Yan L, Huang Q, Zhang D, Zhao Y, Zhang X (2021) Composite electron transport layer for efficient N-I-P type monolithic perovskite/silicon tandem solar cells with high open-circuit voltage. J Energ Chem 63:461–467. https://doi.org/10.1016/j.jechem.2021.07.018
26. Hyun JY, Yeom KM, Lee S-W, Bae S, Choi D, Song H, Kang D, Hwang J-K, Lee W, Lee S, Kang Y, Lee H-S, Noh JH, Kim D (2022) Perovskite/silicon tandem solar cells with a V_{oc} of 1784 mV based on an industrially feasible 25 cm ^{2} TOPCon silicon cell. ACS Appl Energy Mater 5:5449–5456. https://doi.org/10.1021/acsaem.1c02796
27. PV-magazine (2022) https://www.pv-magaziHZB achieves world record 32.5 efficiency for perovskite tandem solar cell, https://www.Pv-Magazine.Com/2022/12/20/Hzb-Achieves-World-Record-32-5-Efficiency-for-Perovskite-Tandem-Solar-Cell/. Accessed March 2023
28. Saif OM, Elogail Y, Abdolkader TM, Shaker A, Zekry A, Abouelatta M, Salem MS, Fedawy M (2023) Comprehensive Review on Thin Film Homojunction Solar Cells: Technologies, Progress and Challenges. Energies (Basel) 16:4402. https://doi.org/10.3390/en16114402
29. Dänekamp B, Müller C, Sendner M, Boix PP, Sessolo M, Lovrincic R, Bolink HJ (2018) Perovskite-perovskite homojunctions via compositional doping. J Phys Chem Lett 9:2770–2775. https://doi.org/10.1021/acs.jpclett.8b00964
30. Cui P, Wei D, Ji J, Huang H, Jia E, Dou S, Wang T, Wang W, Li M (2019) Planar p–n homojunction perovskite solar cells with efficiency exceeding 21.3%. Nat Energy. 4:150–159. https://doi.org/10.1038/s41560-018-0324-8
31. Wu W-Q, Chen D, Caruso RA, Cheng Y-B (2017) Recent progress in hybrid perovskite solar cells based on n-type materials. J Mater Chem A Mater 5:10092–10109. https://doi.org/10.1039/C7TA02376F
32 Yang D, Zhang X, Wang K, Wu C, Yang R, Hou Y, Jiang Y, Liu S, Priya S (2019) Stable efficiency exceeding 20.6% for inverted perovskite solar cells through polymer-optimized PCBM electron-transport layers. Nano Lett. 19:3313–3320. https://doi.org/10.1021/acs.nanolett.9b00936
33. Hajikhanmirzaei L, Shahroosvand H, Pashaei B, Monache GD, Nazeeruddin MK, Pilkington M (2020) A cost-device efficiency balanced spiro based hole transport material for perovskite solar cells. J Mater Chem C Mater 8:6221–6227. https://doi.org/10.1039/D0TC00196A
34. Kung P, Li M, Lin P, Chiang Y, Chan C, Guo T, Chen P (2018) A review of inorganic hole transport materials for perovskite solar cells. Adv Mater Interfaces 5:1800882. https://doi.org/10.1002/admi.201800882
35. Okil M, Shaker A, Ahmed IS, Abdolkader TM, Salem MS (2023) Design and analysis of Sb2S3/Si thin film tandem solar cell. Sol Energy Mater Sol Cells 253:112210. https://doi.org/10.1016/j.solmat.2023.112210
36. Okil M, Shaker A, Salah MM, Abdolkader TM, Ahmed IS (2023) Investigation of polymer/Si thin film tandem solar cell using TCAD numerical simulation. Polymers (Basel) 15:2049. https://doi.org/10.3390/polym15092049
37. Hedayati M, Olyaee S (2022) High-efficiency p-n homojunction perovskite and CIGS tandem solar cell. Crystals (Basel) 12:703. https://doi.org/10.3390/cryst12050703
38. Silvaco Inc (n.d.) Atlas User's Manual, https://Silvaco.Com/Products/Tcad/Device_simulation/Atlas/Atlas.html. Accessed August 2022
39. Burgelman M, Nollet P, Degrave S (2000) Modelling polycrystalline semiconductor solar cells. Thin Solid Films 361–362:527–532. https://doi.org/10.1016/S0040-6090(99)00825-1
40. I. COMSOL (n.d.) "COMSOL Multiphysics Reference Manual, version 5.3", www.Comsol.Com. Accessed June 2023
41. Liu Y, Sun Y, Rockett A (2012) A new simulation software of solar cells—wxAMPS. Sol Energy Mater Sol Cells 98:124–128. https://doi.org/10.1016/j.solmat.2011.10.010
42. Haug A (1978) Auger coefficients for highly doped and highly excited semiconductors. Solid State Commun 28:291–293. https://doi.org/10.1016/0038-1098(78)90646-4
43. Slotboom JW (1977) The pn-product in silicon. Solid State Electron 20:279–283. https://doi.org/10.1016/0038-1101(77)90108-3
44. Zhou Y, Wang F, Cao Y, Wang J-P, Fang H-H, Loi MA, Zhao N, Wong C-P (2017) Benzylamine-Treated Wide-Bandgap Perovskite with High Thermal-Photostability and Photovoltaic Performance.

Adv Energy Mater 7:1701048. https://doi.org/10.1002/aenm.201701048
45. Jannat F, Ahmed S, Alim MA (2021) Performance analysis of cesium formamidinium lead mixed halide based perovskite solar cell with MoOx as hole transport material via SCAPS-1D. Optik (Stuttg) 228:166202. https://doi.org/10.1016/j.ijleo.2020.166202
46. Azri F, Meftah A, Sengouga N, Meftah A (2019) Electron and hole transport layers optimization by numerical simulation of a perovskite solar cell. Sol Energy 181:372–378. https://doi.org/10.1016/j.solener.2019.02.017
47. Prathapani S, Bhargava P, Mallick S (2018) Electronic band structure and carrier concentration of formamidinium–cesium mixed cation lead mixed halide hybrid perovskites. Appl Phys Lett 112. https://doi.org/10.1063/1.5016829
48. Bhardwaj KS, Rai S, Sadanand, Lohia P, Dwivedi DK (2021) Investigating the performance of mixed cation mixed halide-based perovskite solar cells using various hole-transport materials by numerical simulation. Opt Quantum Electron. 53:602. https://doi.org/10.1007/s11082-021-03262-7
49. Kumar M, Raj A, Kumar A, Anshul A (2020) An optimized lead-free formamidinium Sn-based perovskite solar cell design for high power conversion efficiency by SCAPS simulation. Opt Mater (Amst) 108:110213. https://doi.org/10.1016/j.optmat.2020.110213
50. Deng Q, Li Y, Chen L, Wang S, Wang G, Sheng Y, Shao G (2016) The effects of electron and hole transport layer with the electrode work function on perovskite solar cells. Mod Phys Lett B 30:1650341. https://doi.org/10.1142/S0217984916503413
51. Kirchartz T, Cahen D (2020) Minimum doping densities for p–n junctions. Nat Energy 5:973–975. https://doi.org/10.1038/s41560-020-00708-2
52. Salem MS, Saif OM, Shaker A, Abouelatta M, Alzahrani AJ, Alanazi A, Elsaid MK, Ramadan RA (2021) Performance optimization of the InGaP/GaAs dual-junction solar cell using SILVACO TCAD. Int J Photoenergy. 2021. https://doi.org/10.1155/2021/8842975
53 Amri K, Belghouthi R, Aillerie M, Gharbi R (2021) Device optimization of a lead-free perovskite/silicon tandem solar cell with 24.4% power conversion efficiency. Energies (Basel). 14:3383. https://doi.org/10.3390/en14123383
54 Bacha M, Saadoune A, Youcef I, Terghini O (2022) Design and numerical investigation of Perovskite/Silicon tandem solar cell. Opt Mater (Amst). 131:112671. https://doi.org/10.1016/j.optmat.2022.112671